Numerical Study on the Operating Limits of MPD Thrusters

IEPC-2013-182

Presented at the 33rd International Electric Propulsion Conference,
The George Washington University • Washington, D.C. • USA
October 6 – 10, 2013

Arsad Quraishi[1] and M.Mahendhran [2]
Indian Institute of Technology Madras, Chennai-600036, India

Amit Kumar[3]
Indian Institute of Technology Madras , Chennai-600036, India

The effect of thruster operating limits of coaxial and two-dimensional (2D) self-field Magnetoplasmadynamic (MPD) thrusters is studied using a numerical model. The plasma flow in the thruster is modeled as inviscid, compressible, fully ionized perfect gas flow. The flow and electromagnetic field equations (derived from Maxwell's equations), which govern the plasma flow, are discretized using a finite volume approach. The validated numerical code is used to simulate 2D and thrust equivalent coaxial MPD thrusters.

The thruster operation shifts from thermal regime at low currents to electromagnetic regime at high currents in a similar manner for both 2D and coaxial thrusters but, the maximum (limiting) current after which the numerical instability occurs is higher for coaxial thruster compared to 2D thruster. Interestingly the limiting current was found to occur at about a nearly constant specific impulse which was significantly higher for the thrust equivalent coaxial thruster. It was also noted for both 2D and coaxial geometries, while short cathodes give better performance compared to long electrodes, the long electrode configuration can operate stably at higher specific impulse.

Nomenclature

2D	=	two-dimensional
Δx	=	grid size in x-direction
α	=	co-efficient to specify the amount of current through cathode tip
β	=	electron Hall parameter
ε_0	=	permittivity of free space (=8.854×10^{-12} farad/m)
μ_0	=	magnetic permeability of free space (=$4\pi\times 10^{-7}$ henry/m)
κ	=	Boltzmann constant (=1.38×10^{-23} J/K)
ρ	=	density
σ	=	electrical conductivity
ω_e	=	gyro frequency of electrons
τ_e	=	collision time of electrons
$\mathbf{B}$	=	self induced magnetic field
B_0	=	self induced magnetic field at inlet
d	=	diameter

[1] M.S. Scholar, Department of Aerospace Engineering, arsadscorpio@gmail.com
[2] M.S. Scholar(graduated) Department of Aerospace Engineering, mmahendhran@gmail.com
[3] Associate Professor, Department of Aerospace Engineering, amitk@ae.iitm.ac.in

e = charge of a proton (=1.602× 10^{-19} C)
e_t = total specific energy of the fluid
E = electric field
F = thrust
g_0 = gravitational acceleration on earth (=9.81 m/s^2)
I = input current
I_{sp} = specific impulse
j = current density
$\dot{m}$ = inlet mass flow rate
M = Mach number
MPDT = Magnetoplasmadynamic Thruster
n = outward normal vector
n_e = number density of electrons
p = pressure
R_{gas} = specific gas constant
r,θ,x = cylindrical coordinates
t = time
T = temperature
v = velocity vector (u, v components)
W = width of the channel in 2D MPDT
x,y,z = Cartesian coordinates

Subscripts
a = anode
c = cathode
coax = coaxial
em = electromagnetic

Introduction

Magnetoplasmadynamic (MPD) thrusters are electromagnetic class of electric propulsion thrusters. They are capable of delivering high specific impulse (I_{sp}) and thrust at high input power along with the flexibility to operate at various power levels. Therefore, MPD thrusters exhibit potential for long-range space flight missions such as interplanetary travel and also for typical missions such as orbit transfer etc.

There have been various analytical, experimental and numerical studies that bring out the effect of thruster geometry and configuration on its performance[1-6] (Thrust and I_{sp}). These studies report an increase in performance with the shortening of cathode implying that the geometric configuration of thruster has an effect on its performance. This article presents some of the interesting observations resulting from a comparative study on 2D and thrust equivalent coaxial thruster geometry at various operating conditions.

An outline of formulation and numerical methodology used to develop the 2D and coaxial MPD thruster model is presented concisely in following sections for completion. A detailed description of the model can be found in Ref. 7.

Formulation

The plasma flow in the thruster is modelled based on some typical assumptions and by using generic governing equations to simulate important physical processes in the thruster. Argon (propellant) is assumed to be completely singly ionized and quasi-neutral plasma as it enters the thrust chamber. It is considered inviscid and thermally non-conducting perfect gas. Further, the plasma flow is two-dimensional (x-y plane) and the magnetic field acts only in third (z) direction for 2D-MPDT. In coaxial MPDT, the flow is axisymmetric (x-r plane) and magnetic field acts only in the azimuthal (θ) direction.

The integral form of mass, momentum and energy equations for inviscid, compressible flow with electromagnetic body forces and joule (ohmic) heating included as momentum and energy source terms are taken as governing equations of plasma flow. Maxwell's equations and Ohm's law are combined to form a single equation in terms of magnetic field to model the currents, electric and magnetic field in the thruster. The above stated governing equations are presented below.

Mass conservation equation:
$$\frac{\partial}{\partial t}\int_{\Omega}\rho d\Omega+\oint_{s}\rho\mathbf{v}\cdot\mathbf{n}ds=0 \tag{1}$$

Momentum Equation:
$$\frac{\partial}{\partial t}\int_{\Omega}\rho\mathbf{v}d\Omega+\oint_{s}\rho\mathbf{v}\mathbf{v}\cdot\mathbf{n}ds=-\oint_{s}p\mathbf{n}ds+\int_{\Omega}\mathbf{j}\times\mathbf{B}d\Omega \tag{2}$$

Energy Equation:
$$\frac{\partial}{\partial t}\int_{\Omega}\rho e_t d\Omega+\oint_{s}(\rho e_t+p)\mathbf{v}\cdot\mathbf{n}ds=\int_{\Omega}\mathbf{j}\cdot\mathbf{E}d\Omega \tag{3}$$

Equation of State:
$$p=\rho R_{gas}T \tag{4}$$

Combining Ampere's law and Faraday's law in Maxwell's equation with Ohm's law, a single equation in terms of magnetic flux density is used.

Ampere's law:
$$\nabla\times\mathbf{B}=\mu_0\mathbf{j} \tag{5}$$

Faraday's law:
$$\nabla\times\mathbf{E}=-\partial\mathbf{B}/\partial t \tag{6}$$

Ohm's law:
$$\mathbf{j}=\sigma[\mathbf{E}+\mathbf{v}\times\mathbf{B}-\beta(\mathbf{j}\times\mathbf{B})] \tag{7}$$

Equation of Magnetic flux density:
$$\frac{\partial\mathbf{B}}{\partial t}-\nabla\times(\mathbf{v}\times\mathbf{B})+\nabla\times(\frac{1}{\sigma\mu_0}\nabla\times\mathbf{B})+\nabla\times(\frac{\beta}{\mu_0}(\nabla\times\mathbf{B})\times\mathbf{B})=0 \tag{8}$$

Electrical conductivity for fully ionized plasma is given by Spitzer-Harm formulation

$$\sigma=1.5\times10^{-2}\frac{T^{3/2}}{\ln\Lambda} \tag{9}$$

Where Coulomb logarithm $\ln\Lambda$ is $\ln\Lambda=\ln\left[\frac{12\sqrt{2}\pi\varepsilon_0^{3/2}(\kappa T)^{3/2}}{e^3 n_e^{1/2}}\right]$

The electron Hall parameter is taken as[8,9]

$$\beta=\frac{\omega_e\tau_e}{|B|\sigma}=\frac{1}{en_e} \tag{10}$$

All the variables in the above equations are non-dimensionalized with chosen reference quantities and the governing equations in non-dimensional form are used for the numerical solution.

Numerical Methodology

The governing equations taken in non-dimensional form are discretized using a dual-control volume finite volume method. For the flow equations, central scheme with Jameson's artificial dissipation is used to compute convective fluxes. After spatial discretization the equations become ODEs in time. Then they are integrated using an explicit four-stage Runge-Kutta method.

The magnetic field equation is discretized using a central (averaging) type scheme. The gradient terms are computed based on Green's theorem. The spatially discretized ODE is integrated in time using ADI (Implicit Euler) method. Thomas algorithm is used for the solution of tri-diagonal form of equations. The magnetic field equation is solved separately at each flow time step and the electric and magnetic fields are coupled to the flow equation through momentum and energy source terms.

Only top half of the thruster is modeled assuming flow symmetry about the longitudinal axis. Separate boundary conditions are used to obtain the solution of flow and electromagnetic equations. Subsonic/supersonic inflow, slip wall, centerline symmetry and supersonic outflow are the flow boundary conditions used. Boundary conditions for the electromagnetic equations simulate a constant current at inlet and current conducting electrode surfaces (anode and cathode). Other walls, symmetry plane and exit boundary are considered as non-conducting surfaces.

The convergence of numerical solution is monitored using L2 norm residuals of flow equations and electromagnetic induction equation (at each flow time step). In addition, L∞ norm error in pressure and the difference in net mass flow rate crossing the domain boundaries are also monitored.

Typical thruster parameters such as thrust, its various components (momentum, pressure, thermal and electromagnetic), I_{sp} and input power are calculated from the flow field data. The numerical model of 2D and coaxial thrusters are validated separately against available experimental and numerical results in the literature. The validation details can be found in Ref. 7.

Results and Discussion

A 2D thruster with its dimensions similar to experimental straight-anode thruster[4] is taken as the base geometry for this study. Although the experimental thruster consists of only a straight anode, in the computational model a diverging insulator section is fixed at exit to avoid an abrupt expansion region that could cause numerical instability to the inviscid flow model. This diverging section also converts any available pressure thrust into momentum component.

The theoretical electromagnetic thrust as a function of current and geometry for a 2D thruster[4] and a coaxial thruster[8] are

$$F_{em,2D} = \frac{\mu_0 I^2}{4W}\left(\frac{(d_{a,2D} - d_{c,2D})}{2} + \alpha\frac{d_c}{2}\right) \qquad (11)$$

$$F_{em,coax} = \frac{\mu_0 I^2}{4\pi}\ln\left(\frac{d_{a,coax}}{d_{c,coax}} + \frac{3}{4}\right) \qquad (12)$$

The second term in the above expressions represents cathode tip contribution to thrust. Neglecting this term and equating the above expressions, we obtain an expression for the anode diameter for coaxial thruster.

$$d_{a,coax} = \exp\left(\frac{(d_{a,2D} - d_{c,2D})\pi}{2W}\right) \times d_{c,coax} \qquad (13)$$

The 2D thruster has the following dimensions: $d_{a,2D}$ = 28 mm, $d_{c,2D}$ = 8 mm and W = 84 mm. This yields an anode diameter of 11.68 mm for the coaxial thruster.

Figure 1 shows a schematic diagram of thruster, common to both 2D and coaxial geometries. The thruster dimensions are given in Table 1.Equation (13) is used to obtain anode diameter of the coaxial thruster assuming equal cathode length and cathode diameter (height in case of 2D thruster) as the 2D counterpart. The exit diameter (D3) for the coaxial thruster is obtained by considering an equal exit to inlet area ratio as the 2D thruster.

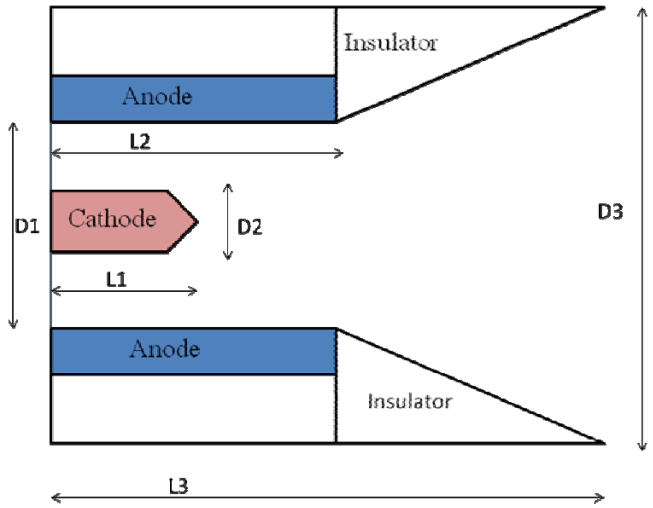

Table 1 Dimensions (in mm) of 2D and coaxial thrusters

Notation	2D	Coaxial
L1	10.0	10.0
L2	50.0	50.0
L3	120.0	120.0
D1	28.0	11.68
D2	8.0	8.0
D3	80.0	19.65

Fig.1 Schematic of the thruster domain

In this study thruster performance is examined over a wide range of operating conditions or control parameters, namely the mass flow rate and the input current. The mass flow rates used are 0.1, 0.3, 0.625, 2.5, 5 and 10 g/s and the input current is varied from a lower limit of 2 kA to a maximum limit specific to each configuration and mass flow rate..

A 151×31 mesh with uniformly spaced grid points was used in most of the computations. For certain cases, the grid points near the inlet were clustered to improve numerical convergence. Numerical instability was observed at low mass flow rates and at high currents, which may be related to the *onset* phenomenon (oscillatory output voltage/potential across the electrodes resulting in the damage of the electrodes), observed in MPDT experiments.

Figure 2 presents contours of total thrust as a function of applied discharge current and inlet mass flow rate for 2D (solid lines) and coaxial (dashed lines) thrusters. The total thrust comprises of electromagnetic thrust (EM body force) and thermal thrust (ohmic heating) components. The total thrust contours are nearly parallel straight lines with a negative slope. The thrust values increase with increase in mass flow rate and increase in current. While increase in thrust with increase in mass flow rate is due to increase in the thermal component, the increase in thrust with

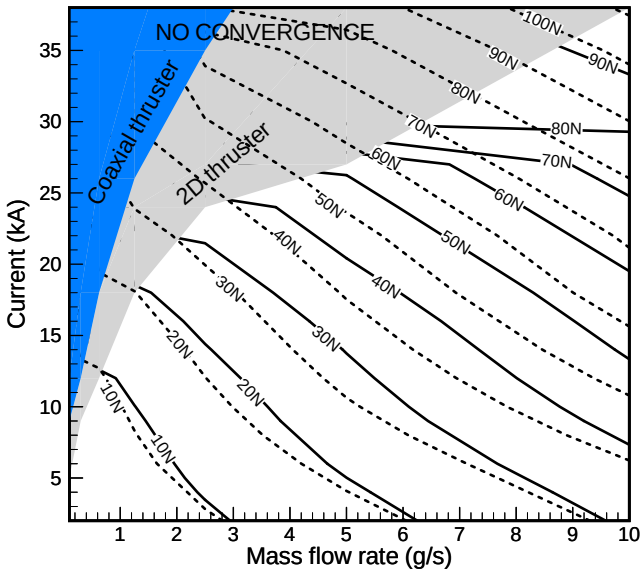

Figure.2 Total thrust contours as a function of current and mass flow rate for 2D thruster (solid lines) and coaxial thruster (dashed lines)

increase in the input current is due to both but primarily due to electromagnetic component, especially at higher currents. The coaxial thruster exhibits slightly higher thrust than the 2D thruster at all currents and mass flow rates. This is due to higher thermal component in case of the coaxial thruster. The shaded regions indicate working limits of the code. Beyond this boundary (in shaded region), a stable numerical solution was not attainable. Interestingly the non-convergence limit is also higher for coaxial thruster compared to 2D thruster.

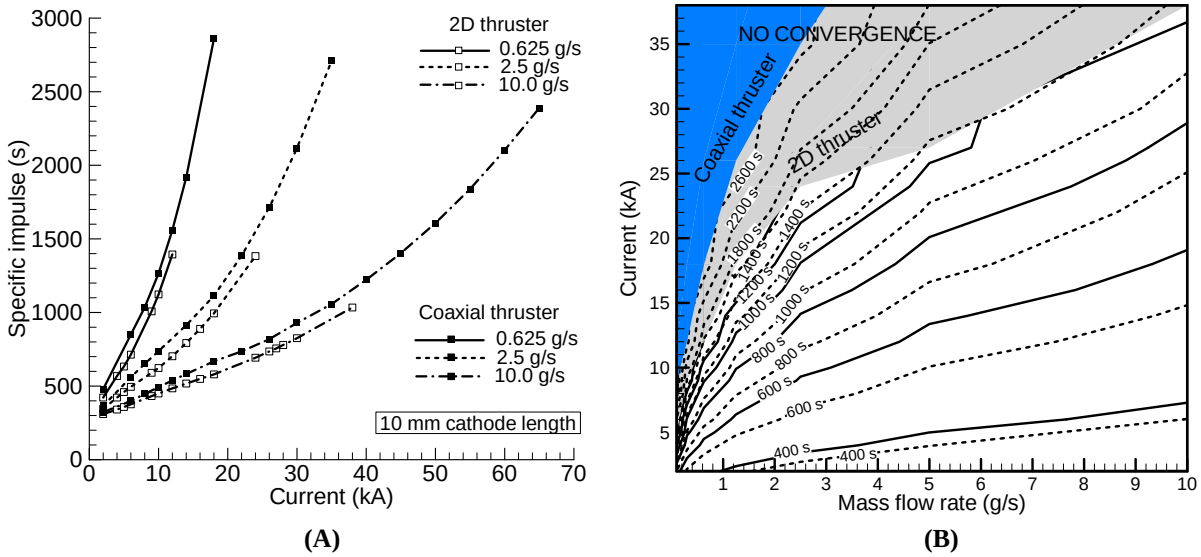

Figure.3 (A) I_{sp} as a function of current at three different mass flow rates (0.625, 2.5 and 10.0 g/s) for 2D and coaxial thrusters. (B) Specific impulse contours as a function of current and mass flow rate for 2D thruster (solid lines) and coaxial thruster (dashed lines)

The plot of I_{sp} as a function of current at various mass flow rates for the 2D and coaxial thruster is shown in figure 3 (A). One can note that although the coaxial thruster exhibits qualitatively similar performance characteristics compared to its 2D counterpart, the coaxial thruster has slightly higher I_{sp} but exhibits a significantly higher

maximum thruster operating limit. Figure 3 (B) shows the operation map with specific impulse contours for 2D (solid lines) and coaxial (dashed lines) thrusters. Specific impulse increases with current, which is expected as $I_{sp} \sim I^2$ and decreases with propellant mass flow rate. One can note that the specific impulse contours closely follow the instability boundary, specifically at low mass flow rates. The I_{sp} contour close to the instability boundary is about 2600s for the coaxial thruster whereas for the 2D thruster it is about 1000-1400s, with the higher values at low mass flow rates.

So far we have seen that the 2D thruster and its thrust equivalent coaxial thruster have nearly identical performance but the numerically determined operation range is much higher for the coaxial thruster. In all these computations the cathode length was 10 mm for both the thruster. Next we look at effect of the cathode length variation on the operating limits for both the thrusters. Additional computations were performed with cathode length increased to50 mm. Figure 4 shows that for both thrusters the long cathode is seen to have higher operating limit (maximum current) and thus more stable compared to the shorter cathode. This implies that other geometrical factors remaining the same, the thruster with long cathodes will allow stable operation at higher specific impulse compared to the thruster with short cathode. In general, well within the operating limits however, it is known that short cathode give somewhat better performance compared to the long electrodes on account of higher thermal thrust component. Comparing the operating limits for long cathode cases for the 2D (Fig. 4(A)) and the thrust equivalent coaxial thruster(Fig. 4(B)), one can again note that the thruster operating limit (maximum current) is higher for the coaxial thruster compared to 2D thruster.

The regime of thruster operation can be classified as electromagnetic and thermal depending upon the dominance of electromagnetic or thermal thrust contribution to the total thrust. Therefore, when electromagnetic thrust is higher than thermal thrust, the thruster is said to be operating in electromagnetic regime and when the thermal thrust dominates over the electromagnetic thrust the thruster is in the thermal regime. Figure 4 shows the two regimes of operation of the thruster on a current-mass flow rate operation map. It can be seen that the thruster operation shifts from thermal regime at low currents to electromagnetic regime at nearly same current values for either cathode length and for both 2D and coaxial thrusters.

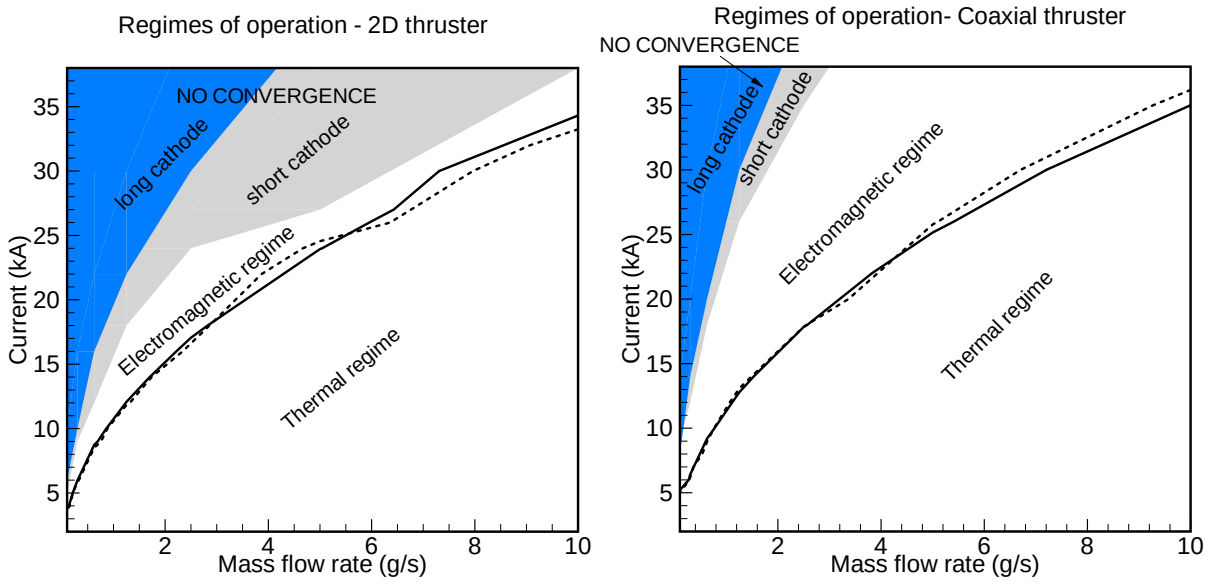

(A) **(B)**

Figure 4 Regimes of operation and operating limits of (A) 2D and (B) coaxial thrusters for short (10mm) and long (50mm) cathodes

The maximum attainable I_{sp} for various thruster configurations as a function of current and mass flow rate are shown in fig. 5 (A) and fig. 5(B) respectively. Here the operating limit of the coaxial thruster can compared with that for the 2D thruster in terms of specific impulse, I_{sp}. The mean value of I_{sp} for short and long cathodes in 2D thruster are 1400 s and 1800 s respectively whereas the I_{sp} values for short and long cathodes in coaxial thruster are 2800 s (there is a single data point which is higher than the other set of points) and 3200 s respectively.

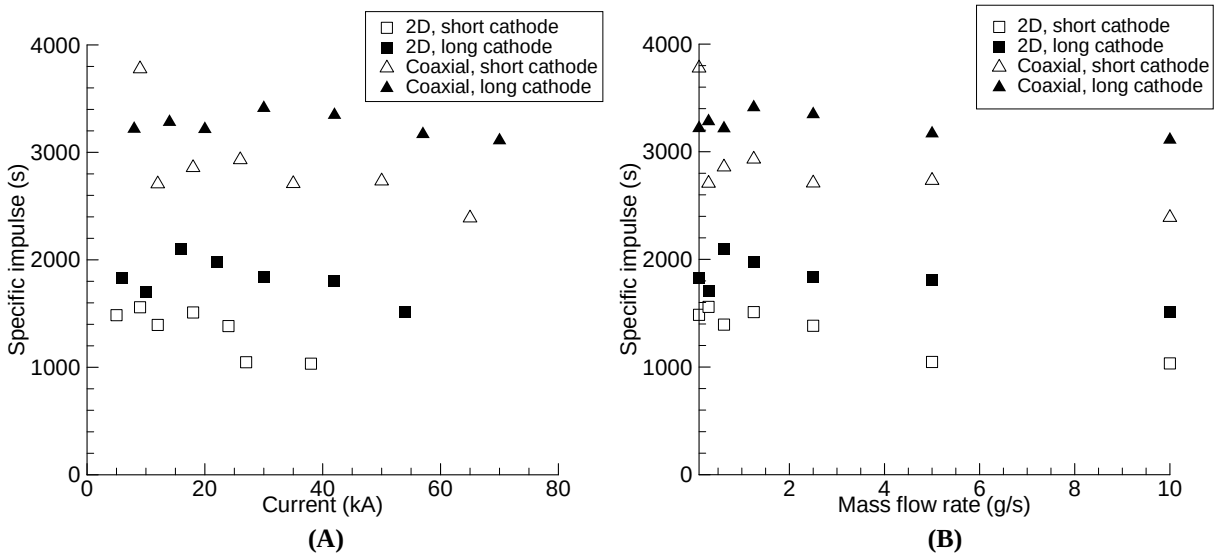

Figure 5 Maximum attainable I_{sp} of 2D and coaxial thrusters (A) as a function of current (B) as function of mass flow rate.

Figure 6 shows the maximum attainable I_{sp} for various thruster configurations as a function of $I^2/\dot{m}$ for all four thruster configurations along with the analytical values. The analytical expressions for I_{sp} are obtained from electromagnetic thrust component.

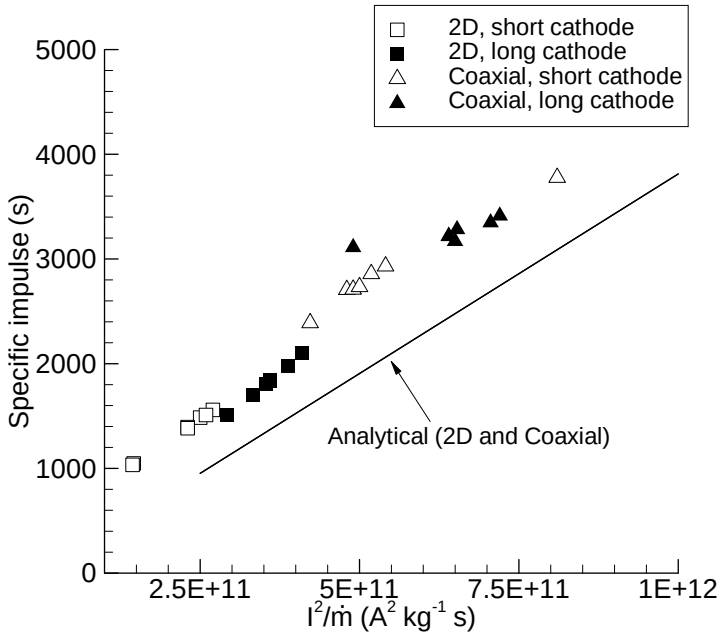

Figure 6 Maximum attainable I_{sp} of 2D and coaxial thrusters as function of $I^2/\dot{m}$

$$I_{sp,2D} = \frac{\mu_0 I^2}{4W\dot{m}g_0}\left[\frac{d_{a,2D} - d_{c,2D}}{2}\right] \quad (14)$$

$$I_{sp,coax} = \frac{\mu_0 I^2}{4\pi\dot{m}g_0}\left[\ln\left(\frac{d_{a,coax}}{d_{c,coax}}\right)\right] \quad (15)$$

The slope of all thruster configurations and the analytical values are nearly equal indicating the identical behaviour of maximum I_{sp} limit with current and mass flow rate in all thruster configurations.But the numerical values are higher than the analytical values, owing to thermal heating in addition to the electromagnetic part. The intercept value of each curve changes, indicating the difference in the range of maximum attainable I_{sp} between each thruster configuration.

Conclusion

The self-field MPD thruster was numerically modeled using 2D and coaxial thruster models. A numerical code was developed to compute 2D/axisymmetric, inviscid, compressible flows. The plasma was modeled as fully ionized perfect gas undergoing electromagnetic interaction with applied current and induced magnetic fields. The code was suitably validated with various MPDT flow field computations. It was then used for a comparative study on 2D and coaxial thrusters.

This study shows that the operating characteristics for 2D and coaxial thrusters are similar in terms of thruster operating regime-i.e. thermal regime at low currents and electromagnetic at high currents. There is also a thermal to electromagnetic regime transition at nearly same currents and mass flow rates.

The difference between 2D and coaxial thruster can be observed in their operating limits. The maximum (limiting) current after which numerical instability occurs is considerably higher for coaxial thruster compared to 2D thruster.

In both 2D and coaxial thruster configurations, long cathode thrusters are more stable compared to short cathodes thrusters at high $I^2/\dot{m}$ i.e. at high currents and low mass flow rates. This implies that long cathodes thrusters are capable of producing higher I_{sp} compared to short cathodes thrusters where the operations of short cathode thruster is likely to be unstable. One should however note that well within the operating limits the short cathode thruster will give a higher I_{sp} at a given operating condition of current and mass flow rate compared to the thruster with long cathode.

References

1. Kuriki, K., Kunii, Y., and Shimizu, Y., "Idealized Model for Plasma Acceleration in an MHD channel", *AIAA Journal*, 21(3), 1983, pp. 322–326.
2. Martinez-Sanchez, M., "Structure of Self-field Accelerated Plasma Flows", *Journal of Propulsion and Power*, 1(7), 1994, pp. 56–64.
3. Nakayama, T., Toki, K., and Kuriki, K., "Quantitative Imaging of the Magnetoplasmadynamic Flow Field", *Journal of Propulsion and Power*, 8(6), 1992, pp. 1217–1223.
4. Funaki, I., Toki K., Kuriki, K., "Electrode Configuration Effect on the Performance of a Two-Dimensional Magnetoplasmadynamic Arcjet", *Journal of Propulsion and Power*, 14(6), 1998, pp. 1043-1048.
5. Funaki, I., Toki K., Kuriki, K., "Numerical Analysis of a Two-Dimensional Magnetoplasmadynamic Arcjet", *Journal of Propulsion and Power*, 13(6), 1997, pp. 789-795.
6. Kubota, K., Funaki, I., and Okunu, Y., "Numerical study of Electrode Geometry Effects on Flow Field in Two-dimensional MPD Thrusters", *Proc. of 30th IEPC*, Paper No. IEPC-2007-87, 2007.
7. Mahendhran, M., Amit Kumar, "Numerical Study on the Effect of Electrode Geometry in MPD Thrusters"**,** Proc. of 32nd IEPC 2011, Paper No.IEPC-2011-228, Wiesbaden, Germany.
8. Jahn, R. G., *Physics of Electric Propulsion*, McGraw-Hill, New York, 1968.
9. Auweter-Kurtz, M., Kurtz, H. L., Schrade, H. O., and Sleziona, P. C., "Numerical Modeling of Flow Discharge in MPD Thrusters," Journal Propulsion and Power, 5, pp. 49-55, 1989.